Seasonal changes in the vertical structure of ozone in the Martian lower atmosphere and its relationship to water vapour.

Kevin S. Olsen, A. A. Fedorova, A. Trokhimovskiy, Franck Montmessin, Franck Lefèvre, Oleg Korablev, Lucio Baggio, Francois, Forget, E. Millour, A. Bierjon, et al.

Seasonal changes in the vertical structure of ozone in the Martian lower atmosphere and its relationship to water vapour.

K. S. Olsen[1], A. A. Fedorova[2], A. Trokhimovskiy[2], F. Montmessin[3], F. Lefèvre[3], O. Korablev[2], L. Baggio[3], F. Forget[4], E. Millour[4], A. Bierjon[4], J. Alday[1,5], C. F. Wilson[1,6], P. G. J. Irwin[1], D. A. Belyaev[2], A. Patrakeev[2], and A. Shakun[2]

[1]Department of Physics, University of Oxford, Oxford, UK.

[2]Space Research Institute (IKI), Moscow, Russia.

[3]Laboratoire Atmosphères, Milieux, Observations Spatiales (LATMOS/CNRS), Paris, France.

[4]Laboratoire de Météorologie Dynamique (LMD/CNRS), Paris, France.

[5]School of Physical Sciences, The Open University, Milton Keynes, UK.

[6]European Space Research and Technology Centre (ESTEC), Noordwijk, Netherlands

Corresponding author: Kevin S. Olsen (Kevin.Olsen@physics.ox.ac.uk)

Key Points:

- Observations of the vertical distribution of ozone on Mars over three years.
- Direct comparison of water vapour, ozone, and temperature, revealing trends and correlations.
- Ozone is observed in higher abundances than photochemical models predict.

Plain Language Summary

Ozone on Mars is part of the so-called odd-oxygen family of reactive, oxidizing gases. It is part of many chemical cycles that help convert one type of gas into another, facilitating the transfer of carbon or hydrogen. Odd-oxygen is crucial to linking the cycles of water vapour and carbon dioxide, or the destruction of trace gases, such as methane. With the Atmospheric Chemistry Suite (ACS) onboard the ExoMars Trace Gas Orbiter (TGO), we are able to study the vertical structure of ozone in the Martian atmosphere and make direct comparisons between it and water vapour and temperature. We have observed ozone abundances several times larger than predicted, suggesting that the oxidizing power of the Martian atmosphere is stronger or faster than expected. We have also observed and measured the relationship between these products: temperature controls the abundance of water vapour, and when the atmosphere cools and water condenses, ozone is able to build up. It is the by-products of when water vapour breaks down in sunlight that remove odd-oxygen from the atmosphere.

This article has been accepted for publication and undergone full peer review but has not been through the copyediting, typesetting, pagination and proofreading process, which may lead to differences between this version and the Version of Record. Please cite this article as doi: 10.1029/2022JE007213.

Abstract

The mid-infrared channel of the Atmospheric Chemistry Suite (ACS MIR) onboard the ExoMars Trace Gas Orbiter is capable of observing the infrared absorption of ozone (O_3) in the atmosphere of Mars. During solar occulations, the 003←000 band (3000-3060 cm^{-1}) is observed with spectral sampling of ~0.045 cm^{-1}. Around the equinoxes in both hemispheres and over the southern winters, we regularly observe around 200-500 ppbv of O_3 below 30 km. The warm southern summers, near perihelion, produce enough atmospheric moisture that O_3 is not detectable at all, and observations are rare even at high northern latitudes. During the northern summers, water vapour is restricted to below 10 km, and an O_3 layer (100-300 ppbv) is visible between 20-30 km. At this same time, the aphelion cloud belt forms, condensing water vapour and allowing O_3 to build up between 30-40 km. A comparison to vertical profiles of water vapour and temperature in each season reveals that water vapour abundance is controlled by atmospheric temperature, and H_2O and O_3 are anti-correlated as expected. When the atmosphere cools, over time or over altitude, water vapour condenses (observed as a reduction in its mixing ratio) and the production of odd hydrogen species is reduced, which allows O_3 to build up. Conversely, warmer temperatures lead to water vapour enhancements and ozone loss. The LMD Mars Global Climate Model is able to reproduce vertical structure and seasonal changes of temperature, H_2O, and O_3 that we observe. However, the observed O_3 abundance is larger by factors between 2 and 6, indicating important differences in the rate of odd-hydrogen photochemistry.

1 Introduction

Ozone (O_3) plays a crucial role in the atmospheric chemistry of Mars. O_3 was first observed by the Ultraviolet Spectrometers on Mariner 7 and 9 (Barth et al., 1973; Barth & Hord, 1971), instruments on Mars Express and the ExoMars Trace Gas Orbiter (TGO) have been able to investigate its relationship with water vapour (Lefèvre et al., 2021), its vertical structure (Khayat et al., 2021; Olsen et al., 2020), and its seasonal evolution (Patel et al., 2021). Ozone is produced via the photolysis of carbon dioxide (CO_2) and subsequent reactive combination of molecular and atomic oxygen. O_3 is disassociated by photolysis, but this pathway does not yield a net change in odd-oxygen (O and O_3) species. Destruction of odd-oxygen most frequently occurs when atomic oxygen reacts with the hydroperoxyl radical (HO_2), a member of the odd-hydrogen family (with H and OH).

Odd-hydrogen molecules are primarily derived from water vapour photolysis and are responsible for stabilising the ratio of carbon monoxide (CO) and carbon dioxide (CO_2). A long standing problem in Martian photochemical modelling is that over long time scales the amount of CO is underestimated (Lefèvre & Krasnopolsky, 2017). The reaction between hydroxyl (OH) and CO maintains the CO_2 mixing ratio of 95.6%. HO_2 and OH are very difficult to observe directly, but their coupling to water vapour (H_2O), which is their source molecule, and with ozone, as the odd-oxygen loss mechanism, allows the monitoring of ozone to be used as a proxy for odd-hydrogen species. Going further, a comparative study of water vapour and ozone can shed insight into several aspects of Martian photochemistry since their changing relative abundance reflect the rates of change of odd-oxygen and odd-hydrogen, which in turn control other Martian atmospheric constituents such as CO, CO_2, HCl, or nitrogen species.

The integrated column abundance of O_3 has been revealed over broad spatial areas and temporal scales by observations from the Earth (Espenak et al., 1991; Fast et al., 2006), the Hubble Space Telescope (Clancy, Wolff, et al., 1996), and by the Mars Color Imager (MARCI) onboard the Mars Reconnaissance Orbiter (Clancy et al., 2016). SPICAM (SPectroscopie pour l'Investigation

des Caractéristiques Atmosphériques de Mars) on Mars Express has been able to produce both vertical profiles and column abundances of O_3 (Lefèvre et al., 2021; Montmessin & Lefèvre, 2013; Perrier et al., 2006). The Ultraviolet and Visible Spectrometer (UVIS) channel of the Nadir and Occultation for Mars Discovery (NOMAD) instrument on TGO has been able to create a high density data set of O_3 number density vertical profiles with fine resolution (Khayat et al., 2021; Patel et al., 2021). These studies have confirmed the expected anti-correlation with water vapour, revealed a strong increase in ozone abundance over the poles during winters, and seasonality characterised by higher ozone abundances reaching to higher altitudes during the aphelion period.

The mid-infrared channel of the Atmospheric Chemistry Suite (ACS MIR) makes fine spectral resolution (separation of ~0.045 cm^{-1}) solar occultation measurements from the near-polar, circular orbit of TGO. This technique has been shown to be sensitive enough to observe the infrared absorption lines of the 003←000 absorption band of O_3 below 40 km. From the same ACS MIR observations, we can also derive coincident mixing ratios of water vapour. The near-infrared channel (ACS NIR) makes simultaneous observations of the same air mass, and provides coincident measurements of temperature and pressure. Herein, we investigate the vertical structure of O_3 revealed by ACS MIR and make direct comparisons with simultaneously measured vertical profiles of water vapour abundance and temperature. In the following sections we will introduce the instrument and analysis methods, present the vertical profiles of O_3, H_2O, and temperature, organised by season and latitude range, compare these results to data from the LMD Mars Global Climate Model (GCM), and discuss the quantized relationship between H_2O and O_3.

2 Materials and Methods

2.1 ACS MIR

The ExoMars Trace Gas Orbiter entered Martian orbit in late 2016, and commenced its nominal science phase in April 2018, midway through Mars year (MY) 34, and just before a global storm began as Mars approached perihelion, and summer began in the southern hemisphere. It carries four scientific instruments: a stereo camera, a neutron detector, and two spectrometer suites to study the composition of the atmosphere. The Atmospheric Chemistry Suite consists of an electronics block and three instrument channels investigating: the thermal infrared (ACS TIRVIM), the near-infrared (ACS NIR), and the mid-infrared (ACS MIR).

ACS MIR is a cross-dispersion spectrometer consisting of a large echelle diffraction grating that provides access to the infrared spectral range, coupled to a secondary diffraction grating that separates the high diffraction orders (Korablev et al., 2018). The secondary grating is steerable, and each position provides access to a specific instantaneous spectral range. The secondary grating position used in this study is 12, which allows us to observe diffraction orders 173-192 covering the spectral range 2850-3250 cm^{-1}. This position contains the spectral features of O_3, HCl, H_2O, and CO_2, and is used in the search for CH_4.

ACS MIR operates in solar occultation mode, making a series of observations of the sun while the atmosphere is between the sun and the spacecraft. Each observation in an occultation sequence is at a unique tangent height, providing a vertical resolution of 1-4 km, depending on the orbital geometry. Spectra are recorded on a two-dimensional detector, over which the *x*-axis corresponds to wavenumber and the *y*-axis separates the diffraction orders. Each diffraction order appears as a stripe over the detector covering around 20 rows. The width of the stripe corresponds to the vertical field of view of the instrument, so each row is a unique transmission

spectrum separated by ~100-200 m (Korablev et al., 2018; Olsen, Lefèvre, et al., 2021; Trokhimovskiy et al., 2020).

The entire sequence of solar occultation observations (one extracted spectrum at each tangent height) is analysed at once to obtain vertical profiles of the target quantities. Observations made above the top of the atmosphere provide a measurement of the solar spectrum, which is used for radiance calibration and to convert solar emission spectra into atmospheric transmission spectra. Example spectra are shown in Figure 1 over the spectral region containing the absorption band of ozone (at wavenumbers where no sunlight is absorbed, the transmission spectra are unity).

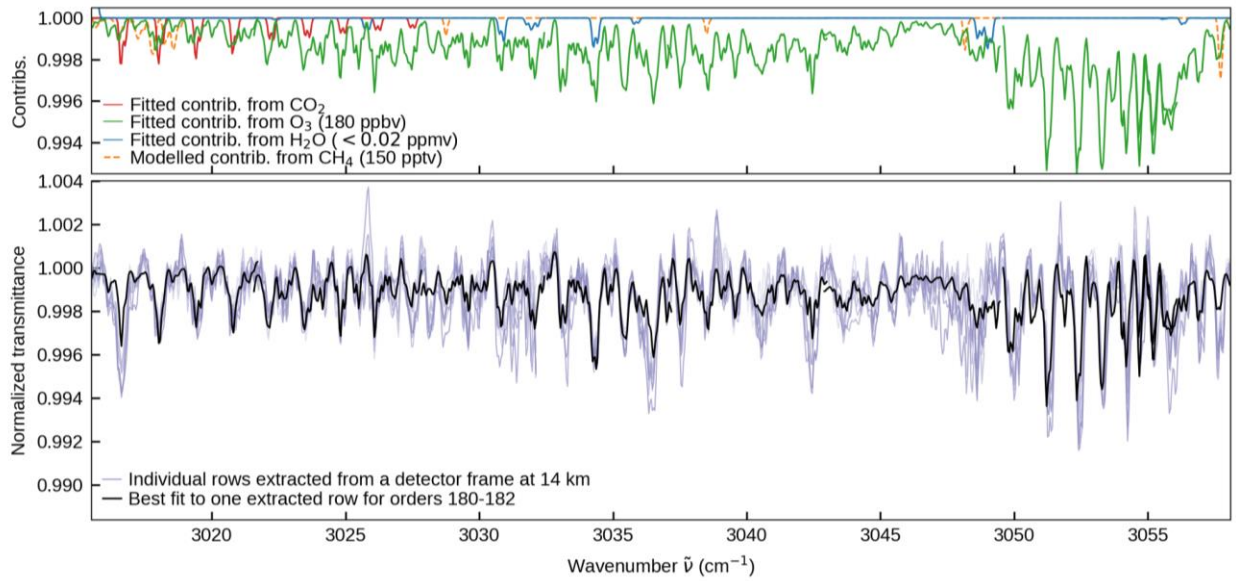

Figure 1. Example ACS MIR spectra showing ozone absorption features. The top panel shows contributions to the best-fit line for different gases. The *P* and *R* branches of the 003←000 vibration rotation band of O_3 are distinct and dominate the spectral range. Water vapour lines are not present and a portion of the newly-identified magnetic dipole band of CO_2 is visible at lower wavenumbers. Also indicated are the locations of CH_4 absorption lines that are targeted in this configuration of ACS MIR. The lower panel shows normalised spectra from orders 180-182 extracted from 11 rows of the ACS MIR detector images (shades of purple) and a best-fit line for one row (black). Each row corresponds to a unique tangent height, separated by ~175 m.

2.2 Retrievals

Vertical profiles of the volume mixing ratio (VMR) of target gases are made using the JPL Gas Fitting Software (GFIT or GGG; Irion et al., 2002; Wunch et al., 2011). At each tangent height (defined relative to the aeroid) and over a specified spectral fitting window, a forward model is computed using volume absorption coefficients derived from the 2020 edition of the HITRAN database (Gordon et al., 2021), *a priori* VMR profiles for various gases, vertical profiles of temperature and pressure, and computed optical path through the atmosphere. Where available, line shape parameters for broadening in a CO_2-rich atmosphere are used (Devi et al., 2017; Gamache et al., 2016; Tudorie et al., 2012; Wilzewski et al., 2016). Spectral fitting is performed using non-linear Levenberg-Marquardt minimisation in which target gas VMR profiles are varied to obtain the best-fit. Temperature and pressure data are obtained from simultaneous

measurements made using the ACS NIR instrument (Fedorova et al., 2020, 2022), which observes strong CO_2 bands upwards of 90 km. *A priori* VMRs of major gases (CO_2, H_2O, O_3) were extracted from the LMD GCM with photochemistry (Lefèvre et al., 2004, 2021) at the local times of the solar terminator for the latitudes and solar longitudes (L_s) of ACS occultations. A set of estimated slant column abundances for all observed tangent altitudes is inverted with calculated slant column paths traced through the atmosphere using a linear equation solver to obtain a retrieved VMR vertical profile. This approach to solar occultation limb observations accounts for each atmospheric layer with decreasing number density along the optical path from the tangent point. This approach was previously used to study CO, O_3 and HCl with ACS MIR (Korablev et al., 2021; Olsen et al., 2020; Olsen, Lefèvre, et al., 2021).

Several studies have been performed using ACS MIR data where a single spectrum close to the edge of the observational slit nearest the centre of the Sun was analysed at each tangent height (e.g. Alday et al., 2019; Korablev et al., 2019; Olsen et al., 2020; Trokhimovskiy et al., 2020), which is very computationally efficient. To improve the sensitivity of ACS MIR when absorption feature depths approach the noise level of a spectrum, such as when studying gases present in only trace amounts, or at higher altitudes, more data from the detector frame can be used. This method was developed to improve the retrievals of the trace gas hydrogen chloride (HCl) (Olsen, Trokhimovskiy, Montabone, et al., 2021), and was used to determine upper limits for phosphine (Olsen, Trokhimovskiy, Braude, et al., 2021). This also helps to mitigate complications arising from a changing instrument line shape (ILS; Olsen, Lefèvre, et al., 2021). There is an optical aberration in the imaging subsystem that can cause absorption lines to appear as a double image, the relative magnitude of which changes across the detector frame and vertical field of view. If the ILS is fitted, temperatures, densities and VMRs can be accurately retrieved from such spectra (Alday et al., 2019; Belyaev et al., 2021; Olsen, Lefèvre, et al., 2021).

Each diffraction order is represented by a stripe across the detector array and upwards of 11 rows can be extracted and analysed. Each row is a unique transmission spectrum with its own tangent height (separated by only 0.1-0.2 km), line depths, noise level, and ILS. Examples of 11 spectra extracted from one frame are shown in Figure 1. Sets of occultation spectra are made by grouping the spectra by row (a set of all the top-most spectra, a set of the second row, etc.), since these should have similar noise levels and ILSs, and VMR vertical profile retrievals are performed on each set. The weighted average of the profiles is taken to be the best estimate of the vertical profile of the target gas VMR, and it is assigned the standard deviation of the weighted mean as an uncertainty. This method has been shown to significantly improve the accuracy of a retrieval (Olsen, Trokhimovskiy, Montabone, et al., 2021), since the impact of any data quality issues for a single spectrum are reduced (spurious features, inaccuracies when measuring quantities such as the solar spectrum, corrupted data, interpolation errors, etc.).

Validation of ACS MIR data is frequently done by making comparisons of water vapour retrievals to those from ACS NIR (Fedorova et al., 2020), and this method, applied to secondary grating positions 11 and 12, has improved the stability of the ACS MIR retrievals, their accuracy, and their agreement with ACS NIR. It is used for both water vapour and ozone retrievals presented here.

3 Observations of O_3 with ACS MIR

The TGO entered Mars orbit in the fall of 2016 and began nominal science operation in April 2018 after an aerobraking campaign to circularise its near-polar orbit. Data taking with ACS MIR began on L_s 163° of MY 34 and has continued through the end of MY 35 and continues in MY 36. Opportunities for solar occultation measurements occur twice per orbit, and secondary grating position 12 is used about 15% of the time.

Figure 2 provides an overview of the ACS MIR O_3 observations (349 vertical profiles). The top panel shows the latitudes of observations as a function of solar longitude. The poleward extent of the observations depends on the angle of the plane of Mars' axial tilt and the sun. This is maximum at the equinoxes when they are perpendicular, and minimum between, when they are aligned and the poles experience polar day or night (which cannot be observed in solar occultation). Ozone is regularly detected towards the poles, as indicated in Figure 2 (top panel), during the equinoxes and during the winters in both hemispheres when its abundance should be highest due to the cold and dry atmospheric conditions. It is never detected during southern

summer due to the wet atmosphere, but is observed in northern summer, which is drier and cooler above 10 km relative to summer in the south.

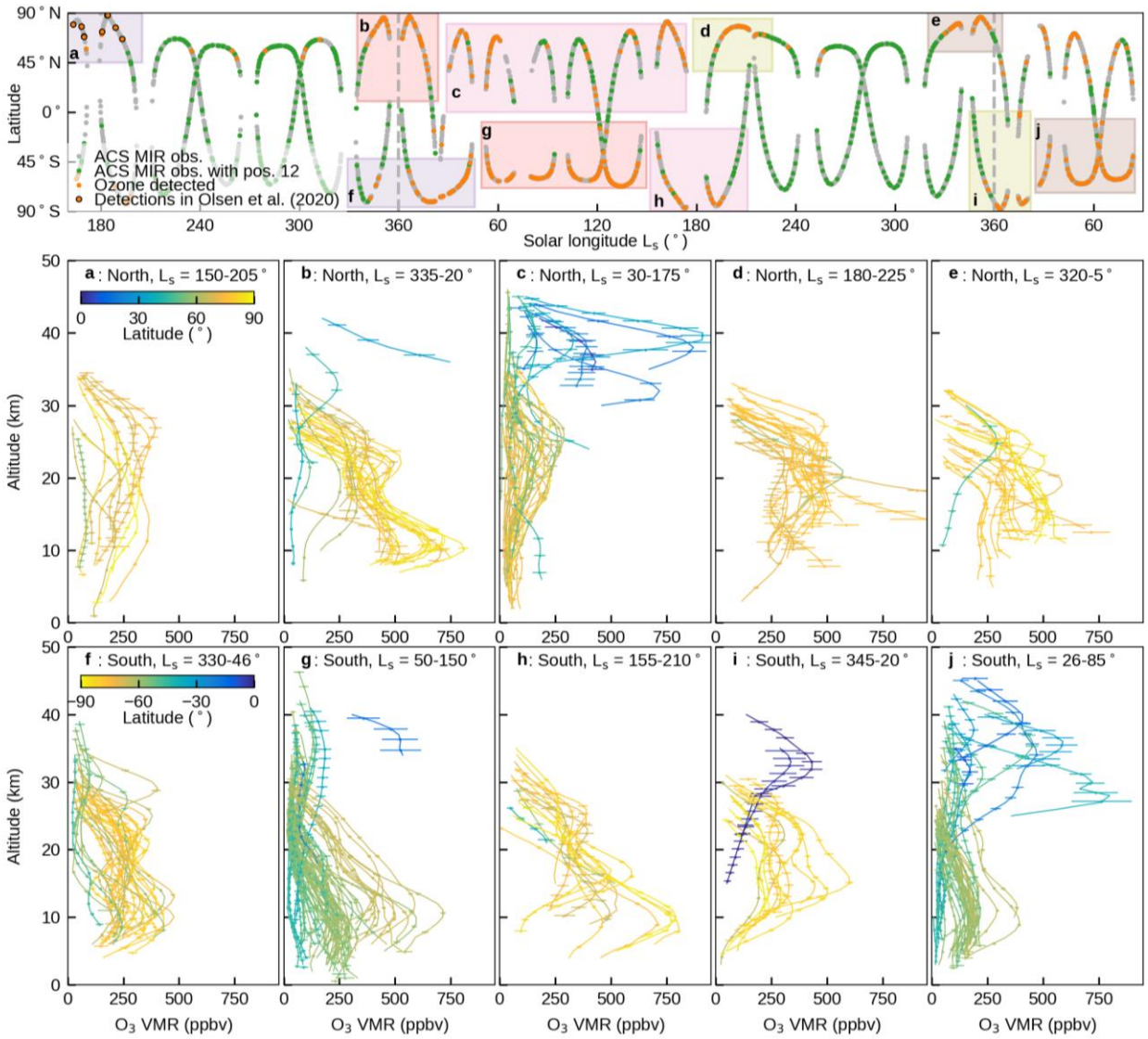

Figure 2. Overview of ozone detections with ACS MIR. The top panel shows the distribution of latitudes probed by ACS over time (solar longitude L_s) since the start of the mission on L_s 163° in Mars year (MY) 34 through to the end of MY 35 and into the beginning of MY 36. All ACS occultations are indicated in grey, those using secondary grating position 12 green, and those with 3σ ozone detections are highlighted in orange. Positive detections are grouped by L_s and latitude, and the retrieved vertical profiles are shown in the lower panels. Panels **a-e** cover the northern hemisphere, and panels **f-j** cover the southern hemisphere.

The lower panels of Figure 2 show the individual retrieved vertical profiles of O_3 VMR. Profiles are grouped by L_s in each panel, and the L_s bounds are indicated in the top panel. The L_s range used for each grouping is based partially on season, but also on the trajectory of the latitudes of observations over time, shown in the top panel. There are four key pieces of information that can be derived from these observations, and they are explored in the following sections, in which we

compare O_3 VMRs to retrieved water vapour abundances and temperatures. The first is that O_3 is very difficult to detect during almost the entire perihelion period between the autumnal and vernal equinoxes (L_s = 220-240°), during which the atmosphere is warm, dusty, and moist in both hemispheres due to the southern summer. Detections in the northern hemisphere are rare, and ozone is not seen in the southern hemisphere. In contrast, O_3 is plentiful at all latitudes in the southern hemisphere during the aphelion period, when it is winter in the south (Figures 2**g**). Thirdly, ozone is most plentiful at high latitudes between seasons (yellow profiles in panels **b**, **d**, **e**, **f**, **h**, and **i** of Figure 2), and finally, an ozone layer near 40 km appears towards the equator during the aphelion period (blue profiles in panels **b**, **c**, **d**, **i**, and **j** in Figure 2). Figure 2 is reproduced in Figure S2 using O_3 data computed with the LMD Mars General Circulation Model (GCM), which is discussed in Section 5 (note that GCM data is only available up to the end of MY 35).

It is expected that there is great variation in O_3 VMRs between day and night, when O_3 photolysis is arrested, and TGO observations are made at either dawn or dusk. However, these diurnal changes are not evident in our data set since over any L_s period, comparing morning and evening observations necessitates a change in hemisphere as well. Local times as a function of L_s are shown in Figure S1. To compare observations made at a morning terminator with those made in the evening, and remaining within the same latitude is generally only possible with observations separated by 10-20° of L_s (20-40 days). Changes observed between evening and morning data must be also considered in terms of changes in latitude and L_s as well, which are much more prominent (note that at lower latitudes where the L_s spacing gets closer, have the higher changes in latitude over time as well).

The data in Figure 2**a** include the initial results reported by Olsen et al., (2020) but reproduced here after three major changes to the analysis method: the results are the mean of analysing 11 spectra; improved estimation of the background signal intensity; and the temperature and pressure used were updated (Fedorova et al., 2020). The shapes of the profiles remain very similar to those published previously in Olsen et al., (2020), but with reduced uncertainties and an extension upwards from 30 to 35 km. The magnitudes of the profiles have changed, but not uniformly, and the approximate O_3 VMR remains around 200 ppbv. Increases in O_3 VMR on the order of 25% are seen after the improvements to the retrievals and data processing. Differences are due to changes in the spectral processing (especially background light calculation) and retrieval algorithm (including the retrievals from multiple rows of the detector frame).

In the following section, we present coincident vertical profiles of O_3 VMR, H_2O VMR, and temperature. We examine first the observations made during the aphelion period at high northern latitudes, then those during the aphelion period at far southern latitudes and high northern latitudes. The transitory periods around the equinoxes and the lower middle to equatorial aphelion observations are also presented. The L_s bounds between these groupings are based on both the shapes and magnitudes of the water vapour and ozone vertical profiles, so chosen to be climatologically similar, as well as the boundaries applied by the periodic changes in solar occultation latitude over L_s.

4 O_3 chemistry in the Martian atmosphere

The Martian atmosphere is characterised in terms of seasons similarly to Earth due to its axial tilt. For example, the northern summer solstice occurs on L_s 90°. Such seasonality is especially visible in nadir observations of its atmosphere, which have provided the dominant view of

contemporary Martian climate (e.g. Clancy, Grossman, et al., 1996; Perrier et al., 2006; Smith, 2004). This includes observations of O_3 which reveal enhancement towards the poles in winters (Perrier et al., 2006). However, nadir observations are sensitive to the lower layers of the atmosphere, and this picture is for altitudes greater than 10 km. Seasonal cycles of temperature and water vapour at altitudes probed by ACS are instead controlled by the orbital eccentricity of Mars, which is much larger than Earth's, revealing north-south symmetries in seasonal cycles (e.g., Aoki et al., 2019; Fedorova et al., 2020).

During the time period surrounding aphelion (L_s = 71°), in which it is approaching summer in the northern hemisphere and winter in the south, warming near the surface over the northern pole leads to the formation of a water vapour layer, but is restricted to below 20 km (Alday et al., 2021). Deep winter cooling over the south pole regions causes condensation of both CO_2 and water vapour on the surface. Conversely, the Martian climate in the period surrounding perihelion is driven by the spring-time sublimation of the southern seasonal ice cap and is characterised by increased atmospheric density, the lifting of dust into the atmosphere, and increased warming of the atmosphere and elevation of the hygropause. Outside regions of polar night or polar day, these effects are global, leading to an atmosphere from 5-60 km that is wetter and warmer during winter than the summer in the northern hemisphere (Alday et al., 2019; Aoki et al., 2019; Fedorova et al., 2020).

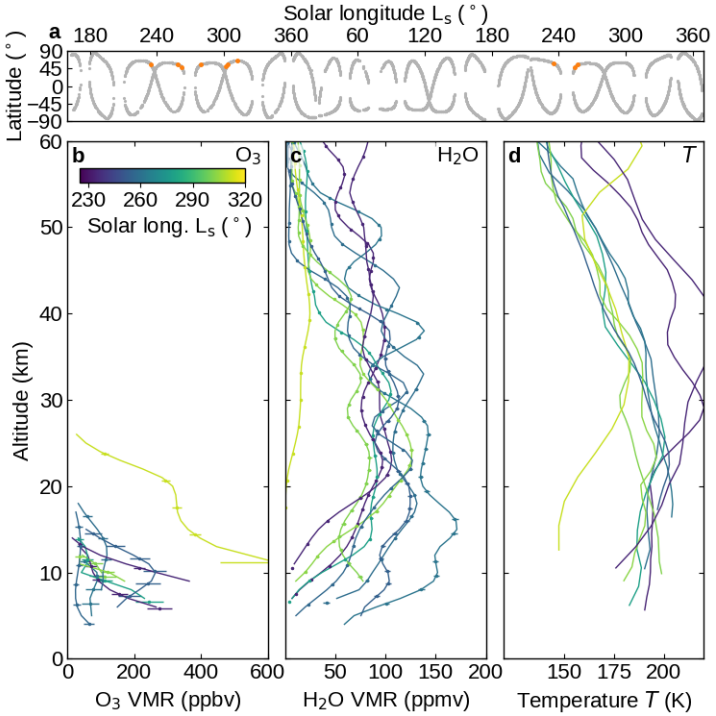

Figure 3. Perihelion ozone observations during northern fall and winter. Panel **a** shows the latitude and L_s of observations, retrieved VMR vertical profiles of ozone (panel **b**) and water vapour (panel **c**) retrieved from ACS MIR, and temperature retrieved from ACS NIR (panel **d**). Colours indicate L_s. These profiles were measured at middle northern latitudes (47°N-66°N) around the perihelion period (northern winter).

ACS MIR observations of O_3 during the perihelion result in very few O_3 detections, with upper limits of ~5-10 ppbv between 10-40 km. In the south during the spring and summer, O_3 is not

detected, and in the north during fall and winter it is rarely detected; and when so, it is almost always in the presence of water vapour. Figure 3 shows the coincident retrieved vertical profiles (above the areoid) measured during the northern winters around perihelion of O_3 VMR from ACS MIR, H_2O VMR from ACS MIR, and temperature from ACS NIR (note ACS NIR data is only available up to the start of MY 36). This novel comparison of coincident data sets along the vertical follows a direct comparison of ozone and water vapour column abundances measured with SPICAM (Lefèvre et al., 2021).

Water vapour is present at VMRs > 100 ppmv above 10 km, but, as these measurements are made towards polar latitudes (but south of 60°N) there is a cold layer below 15 km (Fedorova et al., 2020) causing water to condense and the VMRs to be rapidly reduced below 20 km. This allows ACS to occasionally observe a near-polar ozone layer towards the surface with VMRs between 50-200 ppbv. A polar ozone layer over the surface is expected (Clancy et al., 2016; Perrier et al., 2006), but the lack of detected O_3 in most observations and the presence of H_2O suggests ACS MIR occultations are generally outside the polar vortex, which may extend south to 60°N (e.g., Mitchell et al., 2015; Waugh et al., 2016). Most of these observations occur at 55°N. The polar vortex is not expected to be symmetric and may be sampled irregularly by ACS MIR, depending on Ls and longitude. A notable exception occurred at L_s = 312° and 66°N. This observation reveals a substantially colder atmosphere below 30 km, with very low water vapour, resulting in 200 ppbv O_3 up to 25 km. NOMAD observations in the UV during the time period tend to be restricted to above 20 or 30 km, but reveal a measurable low number density at the lower altitude limits of their observations, and very low abundances above (Patel et al., 2021).

Southern winter observations made during the aphelion period (panel **g** in Figure 2) are shown in Figure 4, which presents vertical profiles of temperature and the VMRs of O_3 and H_2O. These profiles were recorded in the southern hemisphere at latitudes between 55°S and 66°S. In sharp contrast to the northern winter, atmospheric temperatures below 20 km are < 150 K and only rise to 165 K around 30 km. The colder aphelion atmosphere results in much lower VMRs of water vapour by almost an order of magnitude and less than 1.5 ppmv below 20 km. At these latitudes, this allows ozone to remain in the atmosphere below 20 km. While ACS MIR solar occultations do not probe the polar nights during winters, the observed O_3 is likely associated with polar vortex activity, which is expected to be weaker during the southern winters than those in the north, but cover a much broader extent, reaching north of 50°S (Waugh et al., 2016). NOMAD observations from this time and latitude range reveal the highest observed O_3 number densities below 20 km (Patel et al., 2021).

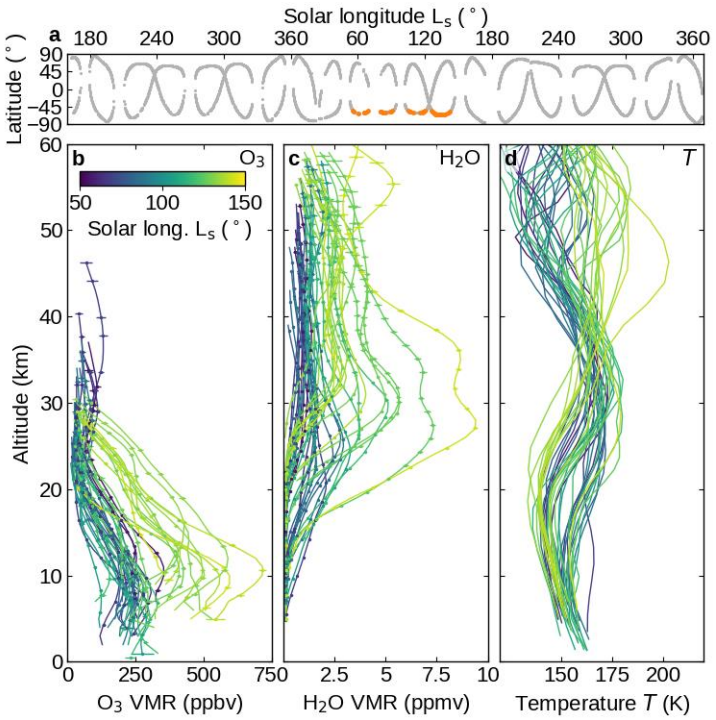

Figure 4. Aphelion ozone observations during southern winter. Panel **a** shows the latitude and L_s of observations, VMR vertical profiles of ozone (panel **b**) and water vapour (panel **c**) retrieved from ACS MIR, and temperature retrieved from ACS NIR (panel **d**). Colours indicate L_s. These profiles were measured at middle southern latitudes (55°S-66°S) during the aphelion period (southern winter) and correspond to Figures 2**g**.

We observe around 200 ppbv O_3 in the lowest layers of the atmosphere, from 15 km to the surface, before L_s = 120°. O_3 decreases towards 20 km, to undetectable levels above 30 km, consistent with observed increases in H_2O VMR from 1 to 5 ppmv at those altitudes. The O_3 enhancement seen at 30 km occurs during a time period in which Montmessin & Lefèvre (2013) reported a layer of O_3 over the south polar region (70°S-80°S) and attributed it to poleward transport of oxygen. Our observations are restricted to higher latitudes, and those early profiles in Figure 4**b** are the northern-most in this data set (towards to 55°S) and more likely related to aphelion cloud belt formation (discussed below).

A portion of the O_3 profiles shown in Figure 4**b** have consistently higher VMRs (brighter green to yellow colours). These are from the latest L_s period in this grouping and were generally recorded at further southern latitudes (brighter yellow colours in Figure 2**g** also). To show this, Figure 4 is reproduced as Figure S3 with the profiles coloured by latitude. For these highest latitude southern winter profiles, we observe also the coldest temperatures in the lower atmosphere, combined with warmer temperatures above 30 km. This results in the largest H_2O VMRs above 30 km, but also peak H_2O VMR gradient and nearly no detectable water vapour below 25 km, leading to higher ozone abundances at these lower altitudes.

Stellar occultation and nadir observations made by SPICAM have been able to show that there are unique mechanisms impacting ozone abundance over the poles during the winter polar nights. SPICAM O_3 vertical profiles during the southern polar winter were compared with GCM simulations to show that transport of high-altitude oxygen-rich air from sunlight regions leads to

an ozone layer forming at 50 km (Montmessin & Lefèvre, 2013). Integrated column abundances, combined with GCM simulations, have shown that H_2O photolysis is no longer responsible for O_3 destruction near the surface (Lefèvre et al., 2021) poleward of ±60°. ACS MIR solar occultations during the perihelion period covering northern winter are not able to verify these mechanisms, however, since they are restricted further south, to the sunlight regions of Mars.

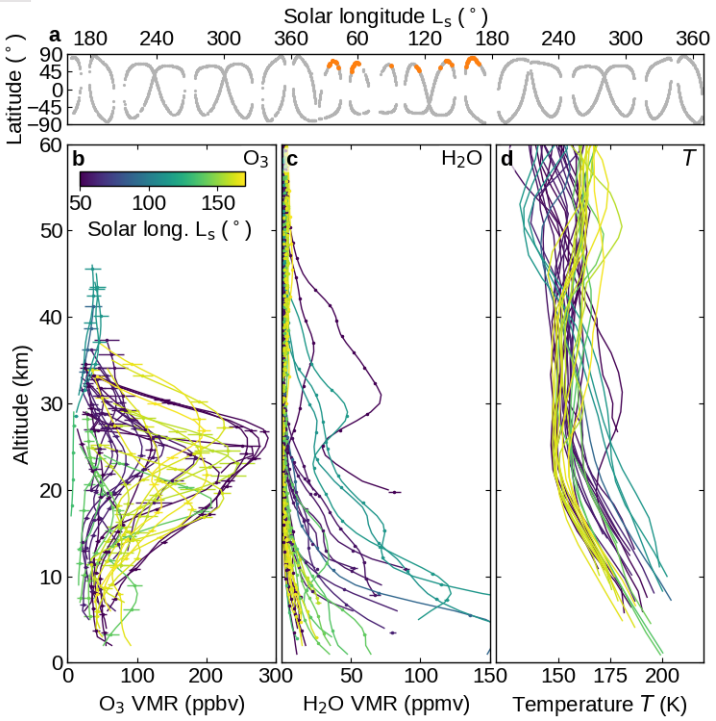

Figure 5. Aphelion ozone observations during northern late spring and summer. Panel **a** shows the latitude and L_s of observations, VMR vertical profiles of ozone (panel **b**) and water vapour (panel **c**) retrieved from ACS MIR, and temperature retrieved from ACS NIR (panel **d**). Colours indicate L_s. These profiles were measured at northern latitudes (55°N-66°N) during the aphelion period (northern summer) and correspond to Figure 2**c**.

During the same L_s period, but in the northern hemisphere, we observed similarly cold temperatures around 20-30 km, resulting in low water vapour abundances and peak ozone abundances. These profiles are shown in Figure 5 and correspond to Figure 2**c**. In contrast to the south, the lower atmosphere has warmed, associated with northern summer, such that water vapour increases near the surface, and ozone is depleted below 20 km. The number densities reported by Patel et al. (2021) do not reveal a decrease in O_3 abundance and observe a more uniform O_3 density up to 50 km. Most ACS observations in which ozone was observed occurred closer to the equinoxes, which was also observed with NOMAD. Observations with maximum O_3 values over this Ls period correspond to the spring (dark blue profiles) and fall (yellow profiles) boundaries of the northern summer solstice. Summer solstice O_3 values (green-blue profiles) are very low since the atmosphere is sufficiently warm during the middle of this L_s period to host water vapour, leading to ozone depletion.

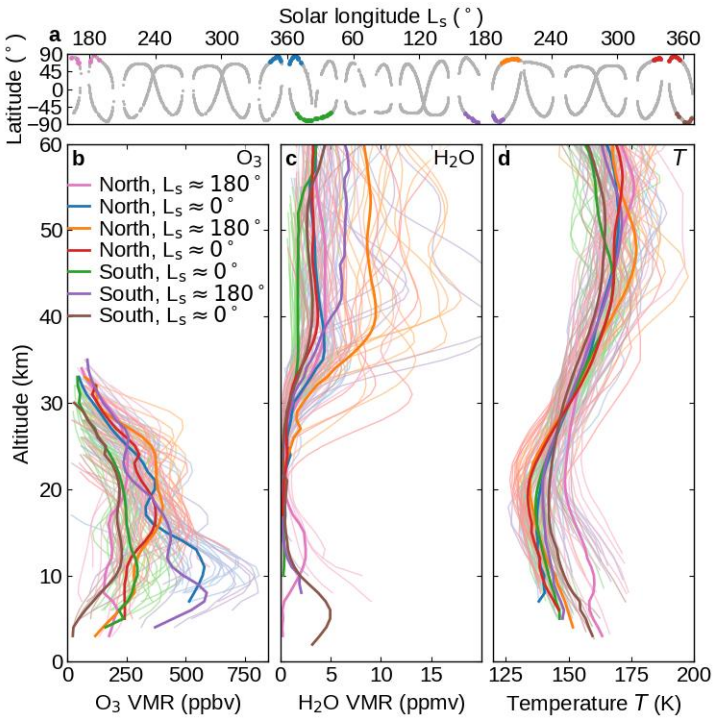

Figure 6. Ozone observations during the equinoctial periods. Panel **a** shows the latitude and L_s of observations, VMR vertical profiles of ozone (panel **b**) and water vapour (panel **c**) retrieved from ACS MIR, and temperature retrieved from ACS NIR (panel **d**). Colours indicate grouping by time period and hemisphere. These profiles were measured towards the north and south poles around L_s 0° and 180° and correspond to panels **b**, **d**, **e**, **f**, **h** and **i** of Figure 2.

TGO solar occultation opportunities probe the furthest towards the poles during the equinoxes when the plane of Mars' axial tilt is perpendicular to the sun, and it is neither polar night nor day. As expected, the periods surrounding the vernal and autumnal equinoxes in the north and south, and to either side of the aphelion periods, exhibit north-south symmetry (Daerden et al., 2019; Fedorova et al., 2021). Figure 6 combines vertical profiles from high northern (65°N-90°N) and far southern (60°S-90°S) latitudes surrounding both the vernal and autumnal equinoxes (panels **a**, **b**, **d**, **e**, **f**, **h** and **i** of Figure 2). These periods are characterised by a cold lower atmosphere, increasing from ~140 K near 20 km to ~165 K above 45 km. Temperatures below 35 km are consistently lower during the equinoxes than those shown in Figure 4**d** from the southern winter (excepting the late southern profiles, yellow in Figure 4**d**, which are in a transition from the aphelion period to the equinoctial period).

Below 30 km, water vapour abundances rapidly fall, revealing a dry lower atmosphere at these near-polar latitudes. This dry, cold, polar lower atmosphere provides conditions for O_3 to remain in the atmosphere, and we consistently record around 200-500 ppbv O_3 from 25 km to the surface.

A comparison between water vapour and ozone around these periods was made using column abundances measured with SPICAM. Around the equinoxes, Lefèvre et al. (2021) noted a significant difference between the retrieved ozone columns in the northern spring (L_s = 0-30°) and northern autumn periods (L_s = 150-180°) using data from SPICAM. This was also visible in the LMD GCM simulations. ACS MIR vertical profiles are able to show why there was a

difference in the column abundances between the spring and autumn observations. In Figure 6, we show that the equinoctial periods near L_s = 0° and L_s = 180° have very similar VMR magnitudes and vertical profile shapes. However, the period L_s = 150-180° identified by Lefèvre et al. (2021) is too early in this season to exhibit such symmetric behaviour. ACS MIR profiles from it are included in Figure 2**a** and **c** (and 5**a**). In contrast to the profiles shown in Figure 2**d** (and 6**a)**, which feature ~400 ppbv O_3 between 10-25 km, the profiles from before L_s = 180° exhibit a sharp decline in O_3 abundance below 25 km. This is due to the late-season persistence of the low-altitude H_2O layer in northern summer visible in Figure 5. In the SPICAM data, the period following L_s = 180° also has low column abundances, but matches those obtained at low southern latitudes, which are in agreement with ACS MIR results that show north-south symmetry at this time. During L_s = 0-30°, SPICAM coverage extends north over the polar vortex region, at the end of a period in which the polar O_3 layer is fully formed and confined below 5 km. Conversely, during L_s = 180-210°, the SPICAM coverage is pushed southward, to the periphery of the polar region and at a time when the polar ozone layer has not yet fully formed. Due to the similarity in ACS MIR profiles from these periods (Figures 2**a**, **c**, and **e**), it is likely that the difference in latitude coverage and the behaviour of O_3 below 5 km is responsible for the discrepancy in column abundances.

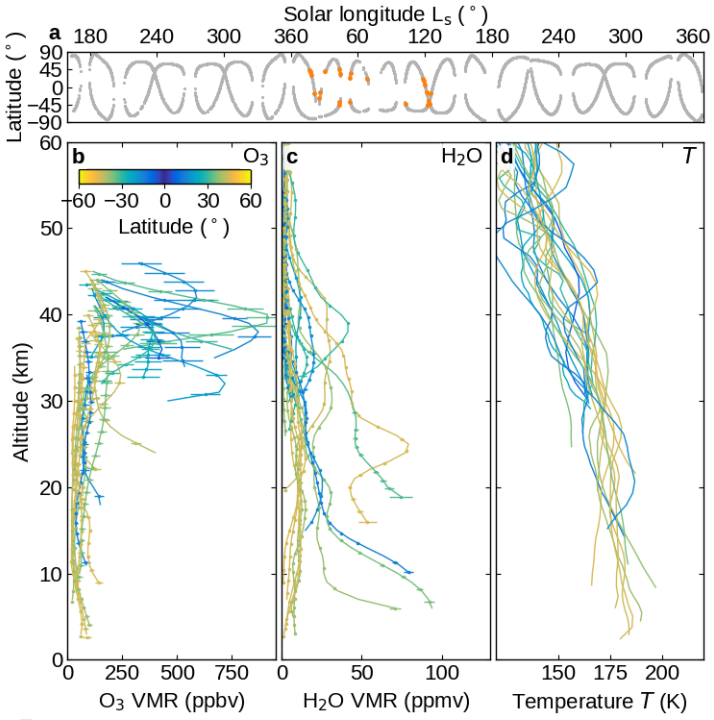

Figure 7. Ozone observations made at equatorial and low middle latitudes during the aphelion period. Panel **a** shows the latitude and L_s of observations, VMR vertical profiles of ozone (panel **b**) and water vapour (panel **c**) retrieved from ACS MIR, and temperature retrieved from ACS NIR (panel **d**). Colours indicate latitude. These profiles were measured at low latitudes (40°S-40°N) during the aphelion period (southern winter/northern summer) and correspond to panels **c** and **g** of Figure 2.

A unique grouping of observations in the ACS MIR solar occultation data set is during the aphelion period, but at latitudes towards the equator in both hemispheres, between 40°S and

40°N. Compared to the other case studies presented here, observations in this period feature a temperature profile exhibiting a uniform gradient from a warm surface (~180 K) to a very cold upper atmosphere (< 130 K at 60 km), shown in Figure 7**c**. This temperature gradient allows for water vapour of varying abundances to be present below 30 km, but only in trace amounts above (Figure 7**b**). At these times and latitudes, when ozone is observable, we note very low abundances below 30 km, which are generally the only altitudes where we otherwise detect ozone in our data. Unique to this L_s range and latitude band, we observe enhancements of ozone of several 100 ppbv at 40 km (Figure 7**a**). This equatorial ozone layer associated with the aphelion cloud belt becomes more pronounced as observations move from low middle latitudes (25°-40°N/S) towards the equatorial region (25°S-25°N).

The change in water vapour abundance observed in Figure 7 is due to condensation and is caused by the temperature gradient along the vertical. This results in the formation of the well known aphelion cloud belt (Clancy & Nair, 1996; Pearl et al., 2001; Smith, 2004). That seasonal cloud formation would impact O_3 abundance was recognized in early photochemical models (e.g. Clancy & Nair, 1996), and this was observed by SPICAM (Lebonnois et al., 2006). The presence of water ice clouds over this period can be inferred from ACS MIR observations. Aerosol attenuation is visible in an ACS MIR solar occultation sequence of spectra, seen as a reduction in transmission level towards lower altitudes (Olsen, Trokhimovskiy, Montabone, et al., 2021). During the aphelion period and the equinoctial periods (Figures 2, 5, and 6) attenuation occurs below 10 or 20 km. Over the equatorial region during the aphelion period (Figure 7), however, we consistently see attenuation due to ice aerosols beginning around 40 km, corresponding to the fall in H_2O VMR at colder temperatures. Separating signals from ice or dust, and quantifying them, is more challenging, but can be accomplished at certain wavelengths when analysing the continuum of the transmittance, whose shape is solely determined by the particulate components and their broad spectral features (Luginin et al., 2020; Stcherbinine et al., 2020).

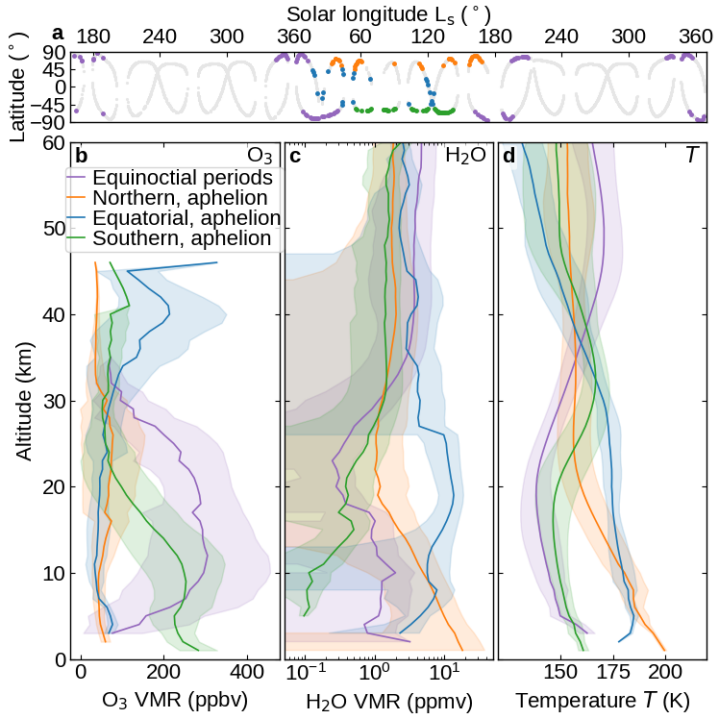

Figure 8. Mean vertical profiles of ozone and water vapour VMRs and temperature from the equinoctial periods (Figure 6), and over the aphelion period in the northern hemisphere (Figure 5), the equatorial region (Figure 7), and the southern hemisphere (Figure 4). The shaded regions indicate one standard deviation of the averaged profiles.

Figure 8 summarises these results by taking the collected profiles in Figure 4-7 and showing their means and standard deviations. During the perihelion period, in which it is summer in the southern hemisphere and dust activity is highest, we are unable to observe ozone at any southern latitudes, and make only occasional observations in the northern hemisphere of low quantities (<200 ppbv) of O_3 below 20 km (around 50°N). In the aphelion period, during northern summer, we are able to observe O_3 below 30 km, but its abundance strongly is reduced rapidly as observations move towards the surface due to increasing temperatures and water vapour over the same altitude range. In southern winter, we make frequent and consistent observations of >100 ppbv O_3 from between 20-30 km to the surface. Between seasons, around both equinoxes in both hemispheres, we observe north-south symmetry in the atmosphere and the highest ozone abundances from 30 km towards the surface.

The comparison is made between O_3 VMR, H_2O VMR and temperature. Temperature controls the condensation of water vapour. Water vapour photolysis leads to HO_2 formation which converts odd-oxygen to stable O_2, effectively reducing O_3 concentrations. The production of O_3 from CO_2 photolysis at these altitudes should not change over time due to the stability of CO_2 concentrations and it being well-mixed. Therefore, the observed changes in O_3 VMRs with latitude and season are the result of changes in its loss rate, directly related to temperature and the VMR of water vapour.

Notably, the highest abundances of O_3 observable by ACS MIR above 30 km (low latitudes aphelion, Figure 7) correspond to the coldest observed temperatures at those altitudes. The

warmest period is the southern and northern hemispheres around perihelion, and corresponds to when O_3 abundances are low to the point where it is difficult to detect. The periods with the highest O_3 VMRs correspond to those in which the lower atmosphere is coldest (equinoctial and southern aphelion, Figures 6 and 4). While the anti-correlation between H_2O and O_3 was anticipated, this is the first direct comparison between the vertical profiles of temperature and the abundances of those two species, revealing the direct impact climate has on odd-hydrogen and odd-oxygen in the Martian atmosphere over different altitudes.

5 O_3 modelled by the LMD GCM

The behaviour of ozone in the Martian atmosphere has been extensively studied by contemporary GCMs. Previous efforts using the LMD GCM have shown it can reproduce SPICAM observations in the polar night through modelled transport and photochemistry (Montmessin & Lefèvre, 2013) ; the Global Environmental Multi-scale (GEM) Mars GCM has been compared to MARCI data (Daerden et al., 2019); and the Open University Mars GCM has been compared to NOMAD data (Patel et al., 2021). However, comparisons with both models to vertical profiles measured with TGO instruments have revealed a discrepancy between the magnitude of modelled and retrieved O_3 VMRs, despite good agreement in O_3 distribution and variability (Khayat et al., 2021; Olsen et al., 2020; Patel et al., 2021). Such discrepancies have been attributed to discrepancies in water vapour abundance which reduces odd-oxygen.

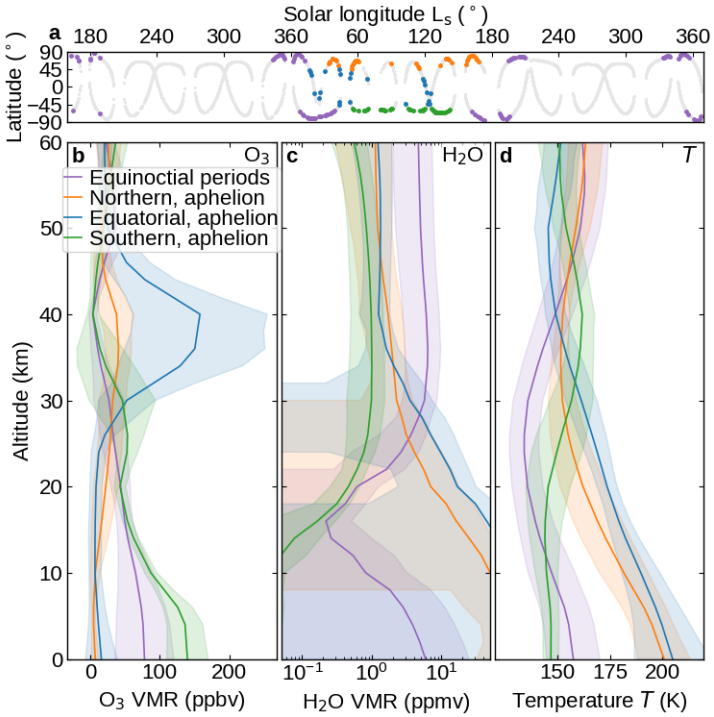

Figure 9. Mean vertical profiles extracted from the LMD GCM. Shown are ozone VMR in panel **b**, water vapour VMR in panel **c**, and temperature in panel **d**, as in Figure 8. Each profile was modelled at the local solar terminator time and location of an ACS MIR solar occultation. Profiles are grouped into the equinoctial periods (Figure 6), and over the aphelion period in the: northern hemisphere (Figure 5), the equatorial region (Figure 7), and the southern hemisphere (Figure 4). The shaded regions indicate one standard deviation of the averaged profiles. Lefèvre et al. (2021) noted that for a given column of H2O, the LMD GCM underestimated

SPICAM O_3 column abundances by about 2 times when using the standard gas-phase chemistry. However, after the inclusion of heterogeneous uptake of OH, HO_2 and H_2O_2 on water ice aerosols was included, differences between the GCM and SPICAM were largely overcome, but these processes remain uncertain .

We use here the latest version of the LMD Mars GCM (Forget et al., 1999) with comprehensive chemistry as described by Lefèvre et al. (2021). The atmosphere has been modelled specifically for TGO solar occultations at local terminator times, taking into account the insolation at the ACS MIR solar occultation points over the boundary of the terminator. In the simulations presented here the GCM was integrated with the nominal gas-phase chemistry, with no heterogeneous uptake of odd-hydrogen by water-ice clouds. Included are dust transport and radiative feedback (Madeleine et al., 2012), water vapour and cloud physics (Navarro et al., 2014). The accuracy of the GCM for a specific Mars year depends on constraints from prescribed climatologies (while dust is transported, its column abundance is forced to follow observations) and this run uses dust climatologies for MY 34 and 35 computed as described by Montabone et al. (2015, 2020). The spatial resolution of the LMD GCM is 3.75° in latitude and 5.625° in longitude (note that the movement of the tangent point due to the orbital movement of TGO is on average 1° in latitude over the lower 45 km altitude). Data are produced in both daily and 5° L_s averaged results, and the latter are used herein.

Figure 9 shows the mean profiles extracted from the GCM at the ACS MIR solar occultation points where O_3 was detected, for comparison with the ACS profiles presented in Figure 8. The different trends seen in each seasonal and latitudinal grouping are clearly visible. In Figure 9**a**, we see that the average ozone VMRs in the GCM are about half those observed, with the magnitudes around the equinoxes and at southern latitudes being around 100 ppbv. ACS MIR observations are >200 ppbv and extend to higher altitudes. The O_3 abundances modelled by the GCM over southern winter are greater than those from the equinoxes, in contrast to ACS MIR observations. Another notable difference is that around northern summer (aphelion) O_3 extends to much higher altitudes in the GCM than the observations. The equatorial ozone layer is very prominent in the GCM data, and the magnitudes of the GCM and the observations are in good agreement, with mean VMRs reaching 200 ppbv.

The magnitudes of low-altitude water vapour also exhibit differences between the GCM and observations. The northern and equatorial regions around aphelion reach ~100 ppmv in the GCM, while ACS MIR observations only revealed ~50 ppmv. The profile shapes are reproduced, as are the VMRs above 10 km. The temperature profiles exhibit the same shapes and magnitudes (Figures 8**c** and 9**c**), with the low-altitude temperatures much warmer in the equatorial and northern regions over the aphelion period (northern summer) than in the south or around the equinoxes. The altitude at which the rate of change is largest (warming or cooling above 30 km), and the subsequent 'pause', is higher in the GCM in each case.

Figure 10 shows a direct quantitative comparison between vertical profiles retrieved using ACS MIR and extracted from the GCM. For each occultation, the vertical profiles from the GCM were interpolated to the pressure levels of the ACS MIR tangent heights where ozone was found. Pressure levels are used rather than tangent heights to mitigate any errors between the estimated heights of ACS MIR and ACS NIR since tangent height is used to define the pressure levels. The comparison is done using number densities rather than VMRs since differences in retrieved VMR may result from differences in temperature and pressure (total number density), rather than measured absorption line depths. Number densities facilitate comparison with Lefèvre et al.

(2021), and since they are monotonic functions of altitude the axes of Figure 10 reveal higher and lower heights. The three panels in Figure 10 show a comparison between the GCM results and water vapour retrieved with ACS MIR data, ozone VMR retrieved with ACS MIR data, and temperature retrieved using ACS NIR data (Fedorova et al., 2020, 2022). The colours are used to group occultations by the latitude and season, as in Figures 4-8.

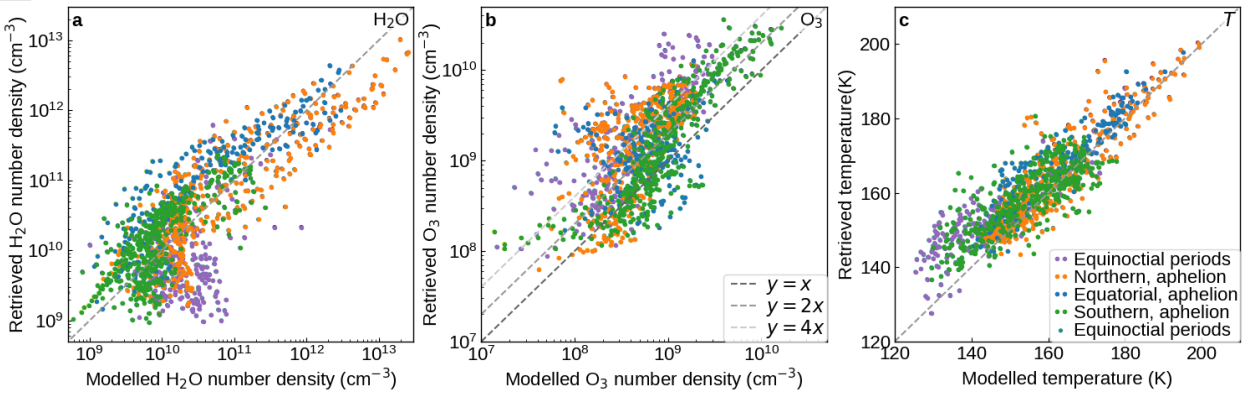

Figure 10. Comparison of H_2O, O_3, and temperature retrieved from ACS data and computed by the LMD GCM. Each retrieved tangent height where O_3 retrievals were made in an occultation sequence are shown. Pressure levels of the profiles extracted from the LMD GCM are interpolated to those of ACS tangent heights. Panels show: **a** H_2O number density retrieved from ACS MIR and modelled by the LMD GCM; **b** O_3 number density retrieved from ACS MIR and modelled by the LMD GCM; **c** temperature retrieved from ACS NIR (Fedorova et al., 2020, 2022) and modelled by the LMD GCM. Dashed grey lines indicated one-to-one correlation. Panel **b** also has lines indicating when the retrieved O_3 values are twice, or 4-times the modelled values. Colours indicate groupings of latitude and season.

In figure 10**a** we see reasonable agreement between water vapour retrieved from ACS MIR and modelled by the GCM, with data generally not showing a bias above or below the line of unity, except during the equinoctial periods. At those times, we are observing less water vapour than the model predicts. Since the pressure range for the comparison comes from the ozone retrievals, these data are restricted to the lower atmosphere, where temperatures and water vapour VMRs were among the lowest measured in this study (Figure 8). The profiles extracted from the LMD GCM reveal a similarly low H_2O VMR with a sharp decrease in water vapour occurring at ~15 km (note that for these ozone number density scales in Figure 10, lower altitudes correspond to higher number densities). However, the LMD GCM predicts larger VMRs above 30 km (> 5 ppmv compared to < 2 ppmv with ACS MIR) and a more prominent surface layer of water vapour, causing the VMR to increase again below 10 km. Due to the relationship between number densities and altitude, large differences in number densities for vertical profiles with similar shapes, as shown in Figures 8 and 9, imply a height mismatch between profile features in the model and observations. Such differences in altitudes where water vapour and ozone are abundant are visible in Figures 8 and 9.

Figure 10**b** shows the number density of ozone retrieved from ACS MIR data and compared to the GCM. ACS MIR generally observes higher ozone concentrations than predicted by the GCM. This tends to occur in each latitude and L_s grouping (but notably so in the equinoctial periods, related to the difference in water vapour described above). The difference tends to be on

the order of 2-6 times greater, depending on altitude and season. The relative differences between the model and observations change over altitude, as can be seen in Figures 8 and 9 (thus we express the difference as a range). The closest agreement occurs in the southern hemisphere around aphelion, when ~200 ppbv O_3 resides below 15 km, and our observations are 1-2 times the GCM. Periods with larger differences are equinoctial periods, where we find a difference of ~4 times. Modelled O_3 over these periods decreases gradually above 10 km, whereas in the ACS MIR observations O_3 remains ~200 ppbv up to 25 km. Around aphelion in the northern hemisphere we observe ~6 times difference. ACS MIR observations reveal ~50-75 ppbv below 30 km, with a peak at 25 km. In the GCM, the ozone abundance peaks at 25 ppbv, but at a higher altitude, 35 km. At lower altitudes, the difference grows, and there is only ~10 ppbv in the model compared to >50 ppbv in the observations. This is the period in which we may be irregularly and indirectly observing the polar vortex, which will not be reflected in the model. Previous studies have found similar disagreement between models and observations, with a factor of 2 times identified in Olsen et al. (2020) and Lefèvre et al. (2021), and up to 10 times in Patel et al. (2021). These results depend on the amount of water vapour present in the model, which was well constrained when examining SPICAM data (Lefèvre et al., 2021). A more important characteristic to compare with the model than ozone abundance, is the anti-correlation with water vapour, which it is now possible to study at discrete altitude levels for the first time with ACS MIR (section 6).

The third panel of Figure 10 shows a comparison between LMD GCM temperature profiles and those retrieved using ACS NIR. These are discussed in Fedorova et al. (2020, 2022). From Figures 8 and 9, we see that ACS observations reveal warmer temperatures in the lower atmosphere. A major difference in these subsets of observations is the height of the observed pauses in Figures 8 and 9. This results in a warmer atmosphere above 20 km in the ACS NIR observations, despite comparable, or cooler, temperatures below. Temperature differences between the model and observations have a direct impact on water vapour, but the variation in whether the GCM is warmer or cooler over the considered altitudes range leads to overall agreement in both temperature and water vapour.

Following our discussion of the shapes of the vertical profiles of these three quantities at different seasons and latitude ranges, shown in Figures 8 and 9, we can see that differences in ozone abundances follow differences in temperature and water vapour abundances. Note that while the LMD GCM was run using MY 35 and MY 36 climate data in the form of solar UV flux and dust opacities, it does not incorporate measured temperatures and pressures, which will further constrain ozone photochemistry. Work is ongoing on assimilating ACS, NOMAD and Mars Climate Sounder Data into the LMD and GEM-Mars GCMs which will allow the reassessment of odd-hydrogen production and ozone reaction rates.

6 Relationships between O_3, H_2O, and temperature

In this section, we will make direct comparisons of the vertical profiles of the VMRs of O_3 and H_2O measured with ACS MIR. Previously, the column abundances of O_3 and H_2O measured with SPICAM over four Martian years have been used to quantify the anti-correlation between these species (Lefèvre et al., 2021). SPICAM viewing geometry allows for observations of polar summers, but not winters, and the best agreement in latitudinal coverage between SPICAM and ACS MIR is around the equinoxes when observations of both instruments extend the furthest poleward (noting that O_3 is not detected with ACS MIR over the perihelion period, and that

SPICAM observations do not extend south of ~40°S over aphelion). Because of the seasonality of O_3, SPICAM coverage is greatest at high northern latitudes (>60°N) over the aphelion period. Distinct trends in the SPICAM O_3 and H_2O comparisons are observed at different time periods, with a stronger reduction in O_3 relative to H_2O observed during northern summer (L_s 60°-150°) than in the spring or equinoxes. The O_3 column abundance relative to H_2O is smaller in the southern hemisphere, although there is symmetry about the autumnal equinox. Coverage is limited in the south because polar winter is not observed and O_3 column abundances in summer are at the detectable limits (< 0.5 μm-atm). No correlation was observed at low-latitudes. The nadir SPICAM observations used to derive column abundances are most sensitive to the lowest layers of the atmosphere and the vertical profiles produced by ACS MIR are able to provide more information about the behaviour of O_3 and H_2O at all altitudes.

The accuracy, vertical resolution, and sensitivity to temperature, pressure, and multiple trace gases of ACS provide a unique opportunity to probe the relationship between different chemical species. The anti-correlation of ozone and water vapour was noted qualitatively in early observations and repeatedly confirmed (e.g., Clancy, Wolff, et al., 1996; Lefèvre & Krasnopolsky, 2017; Perrier et al., 2006 and references therein) and quantified using SPICAM nadir data (Lefèvre et al., 2021). Figure 11 shows the anti-correlation between retrieved water vapour VMRs and retrieved ozone VMRs for the coincident measurements made with ACS MIR at each altitude where ozone was observed. Panels **a** and **b** both contain the same data, with panel **a** showing the uncertainties of the retrieved data and the density of the observations, and panel **b** using colours to indicate the latitude and L_s groupings. Panels **d** and **e** similarly contain the same data, but the upper panels only show data measured above 22.5 km, while the lower panels show data below 22.5 km. A large scatter is revealed by these plots, but the density of the data (Gaussian kernel density estimate using the data contained in both panels **a** and **d**) shows that the majority falls along a straight line indicating an inverse relationship between the VMRs of both gases, and that even when only small amounts of water vapour are present, rapid depletion of ozone is observed. The altitude division between the upper and lower panels shows that all outliers to the main trend visible in panels **a** and **d** come from upper altitudes.

The anti-correlation is not always verified. There is a group of data in the lower middle of Figure 12**a** that lies just below the main trend, with <50 ppbv O_3 and ~1 ppmv H_2O. These were collected in the south during aphelion, at the edge of the dry winter polar vortex. There, observations that were made near 20 km exhibit strong gradients in both the O_3 and H_2O abundances, where ozone is declining and water vapour rapidly increases as altitude grows (Figure 4). Ozone in this period is only observed at low altitudes, around 10 km, and the water vapour is observed to fall rapidly between 20 and 10 km. Another unique subset of observations is that of the equatorial aphelion ozone layer. As water vapour abundance falls and the ozone VMR increases, an apparent minimum water vapour VMR is reached (around 1 ppmv), while the ozone concentration continues to increase above 200 ppbv.

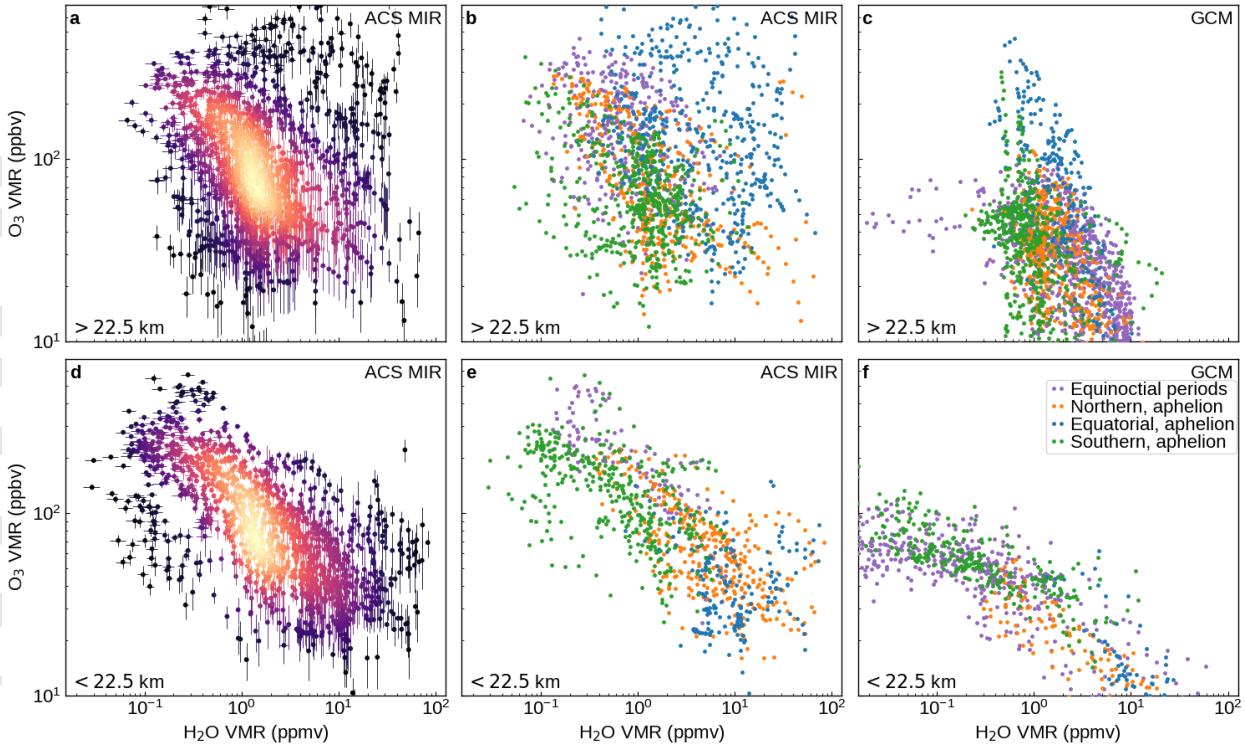

Figure 11. Correlation between water vapour and ozone. Panels **a**, **b**, **d**, and **e** show the simultaneous retrieved O_3 and H_2O data at each tangent height, where both gases were measured by ACS MIR. The upper panels show data from above 22.5 km, while the lower panels show lower altitude data. Panels **a** and **d** include measurement uncertainties and are coloured using a Gaussian kernel density estimate, using the full data set (brighter means high density of data points). Panels **b** and **e** show the same data as panel **a** and **d**, but using colours to indicate the latitude and L_s groupings used in Figures 4-8. Panels **c** and **f** use vertical profiles of H_2O and O_3 VMRs extracted from the LMD GCM for the terminator times at the latitude and L_s of the ACS MIR occultations used in the other panels (coloured as in panels **b** and **e**).

Comparing the data in Figure 11**b** and **e**, distinguished by whether they are from altitudes above 22.5 km or below, we see that when only the lower altitudes are considered the anti-correlation is much tighter. This excludes the altitude range where both O_3 and H_2O are changing relative to one another, and indicates that the altitudes in which VMR gradients are observed have not yet reached a steady state, and there are ongoing processes of photolysis, condensation or sublimation, and chemical reactions.

While the overall anti-correlation is visible in the density plot of the data, the wide variability due to changes in O_3 and H_2O VMRs over altitude, combined with differences between each of the L_s groups leads to low Pearson correlation coefficients, which range from -0.29 to -0.35. Another aspect that affects the anti-correlation that can be explored in the future using a GCM is the impact of local dynamics which would perturb the O_3 and H_2O abundances.

Figures 11**c** and **f** show the same thing, but using the vertical profiles of H_2O and O_3 VMR extracted from the LMD GCM solar occultation run at the latitude and L_s of the ACS MIR occultations. The anti-correlation between water vapour and ozone reveals a similar inverse

trend, but with less ozone being present (and thus a lower slope in panel **c**), by a factor of >2 when considering the maximum values along the trend being ~100 ppbv for the GCM and ~200 ppbv for ACS MIR measurements. A difference of this magnitude was also found between SPICAM and the LMD GCM with only gas-phase chemistry (Lefèvre et al., 2021), and is consistent with the differences between model and observation shown in Figure 10. Of note is that there remains a cluster of data below the main trend. These come from the southern aphelion, with VMRs of H_2O ~1 ppmv and O_3 < 100 ppbv, and are related to altitudes above 30 km where ongoing changes in the VMRs of H_2O and O_3 are seen, and water vapour is increasing. Such cases were noted to be the cause of differences between the model and observation during the equinoctial periods as well. The data in Figures 11**c** and **f** are shown again in Figure S4 coloured by local time, altitude, and latitude.

A second feature that deviates from the trend is the data from the equatorial observations. In the model, the ozone data climb to well over 300 ppbv, but do so in the presence of constant ~1 ppmv of water vapour, unlike other time periods where >100 ppbv of ozone was observed. This occurs at the altitudes where the equatorial ozone layer is observed (see Figure S4 and Figures 8 and 9): the water vapour abundance falls off to <5 ppbv above 30 km, but the O_3 abundance is climbing to 100-400 ppbv. As this is when the aphelion cloud belt is forming, and atmospheric temperatures are continuing to decrease from 30 to 50 km, water ice aerosol formation plays a role in distinguishing the distribution shown in Figure 12**c**. This agrees with the observations shown in Figures 11**b** and **e**, in which the upper right region of the plot is also only populated by data from the equatorial observations. There are a few occultations from the southern aphelion grouping in this region of Figures 11**c** and **f** as well. These were measured around L_s = 54° north of 55°S, the north-most and earliest observations in this grouping, and close to the equatorial grouping.

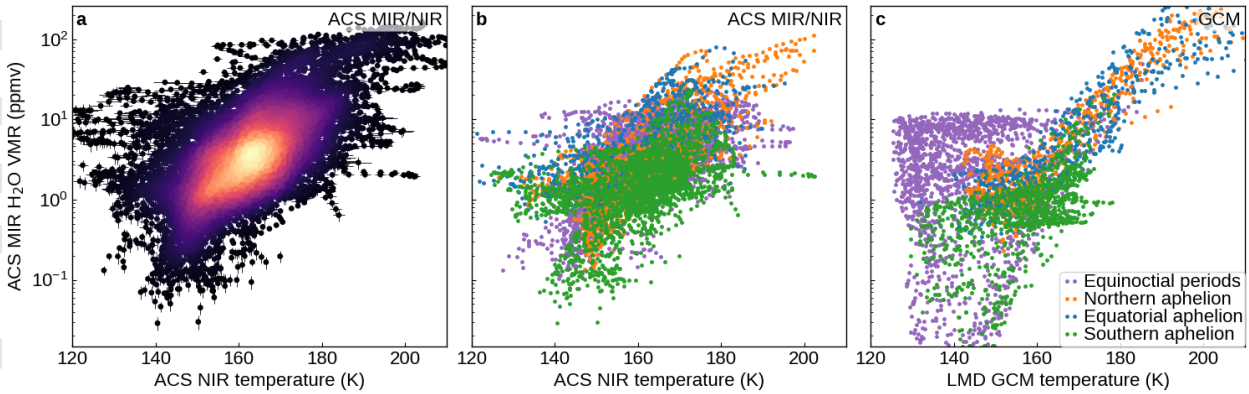

Figure 12. The correlation between water vapour and temperature. Panels **a** and **b** show the retrieved H_2O from ACS MIR and the coincident measurements of temperature made with ACS NIR. The ACS NIR data was interpolated to the pressure levels of the ACS MIR tangent heights. Panel **a** includes measurement uncertainties and is coloured using a Gaussian kernel density estimate (brighter means high density of data points). Panel **b** shows the same data as panel **a**, but using colours to indicate the latitude and L_s groupings used in Figures 4-8. Panel **c** uses vertical profiles of H_2O and O_3 VMRs extracted from the LMD GCM for the terminator times at the latitude and L_s of the ACS MIR occultations used in panels **a** and **b** (coloured as in panel **b**).

In our discussion of Figure 8, we noted that the shape of the ozone profiles appeared to be related

to the temperature of the atmosphere, via the condensation of water vapour. Figure 12 shows the correlation between water vapour retrieved using ACS MIR data and the measured temperature profiles from ACS NIR (Fedorova et al., 2020, 2022). A positive correlation is seen between the two measured quantities, with water vapour increasing exponentially with positive changes in temperature. In the equatorial and equinoctial groupings we observe a minimum amount of water that remains in the atmosphere while temperatures decrease towards some of the coldest temperatures presented here. These cold atmospheric conditions occur above 40 km, where the ozone peak is seen, at low latitudes (Figure 7).

Figure 12**c** again shows the same correlation data, but using profiles extracted from the GCM (and reproduced in Figure S5 showing local times, latitudes, and altitudes). The GCM reveals similar trends as ACS MIR observations, but only for warmer temperatures. Over the equatorial observations, we see a change in the trend as temperatures fall below 150 K. The data in the upper right corner, from low and mid-latitudes in the northern hemisphere, occur at the lowest observed altitudes, where we are observing the warmer summer near-surface layers of the atmosphere (see Figure S5). The southern aphelion data is tightly clustered, as it was when comparing ozone to water vapour in Figure 11, but this time the retrieved data is less clustered than the GCM data. A major difference comes from the equinoctial period observations. In the GCM (Figure 9), descending from 50 km, the temperatures fall from ~180 K to ~130 K, while the H_2O VMRs tend to be fairly constant. From around 30 km towards the surface (Figure 9), temperatures increase again, but the water vapour falls off very rapidly by 20 km due to the cold temperatures. Similar behaviour is observed in the retrievals, but to a lesser extent. A difference between the model data and the retrievals impacting this comparison is that the minimum atmospheric temperature occurs at a lower altitude in the ACS NIR data than in the model computations. The behaviour of water vapour at cold temperatures indicates differences in the model regarding condensation and saturation conditions than in our observations.

7 Conclusions

We present here three years of data collected by ACS MIR on the ExoMars TGO, covering the second half of MY 34, all of MY 35, and the start of MY 36. ACS MIR operating in solar occultation mode is sensitive enough to measure vertical profiles of the VMR of O_3 using the infrared 003←000 absorption band (3000-3060 cm^{-1}). By comparing the vertical structure of simultaneously measured ozone, water vapour, and temperature, we have observed trends in how these important species vary seasonally and exchange hydrogen and oxygen between them. Photochemistry in the Martian atmosphere and the stability of CO and CO_2 depend on odd-oxygen and odd-hydrogen chemistry, and photolysis of H_2O is the primary source of members of the odd-hydrogen family, while O_3 is an important tracer of odd-oxygen.

We have studied the anti-correlation between water vapour and ozone over altitude for the first time, and observed two altitude layers with peak ozone abundance- a near-surface layer present during the cold and dry aphelion period over a wide range of latitudes, and a layer at 40 km over the equatorial region related to the formation of the aphelion cloud belt. Ozone is generally not observed at most latitudes in either hemisphere during the perihelion period, in which the southern summer creates a warm and water-rich middle atmosphere in both hemispheres. Ozone is commonly observed in both hemispheres around aphelion, when it is fall and winter in the south, and spring and summer in the north, with abundances between 200-500 ppbv, which are

generally around 2 times larger than GCM predictions for a given amount of H_2O, but can be greater over specific altitude regions. The northern summer also hosts a near-surface water layer which causes a depletion in ozone below 20 km.

By comparing the vertical structure of ozone, water vapour, and temperature at different latitudes and time periods, we are able to see how the Martian climate controls ozone abundance by varying its rate of destruction, despite the low spatial coverage of solar occultations. Cooling temperatures lead to reduction in the water vapour VMR, and thus a reduction in odd-hydrogen production, which allows O_3 to build up since odd-hydrogen is required to convert odd-oxygen into more stable molecules. The close correlations between temperature and water vapour, and between water vapour and ozone, combined with the observed differences between the expected O_3 abundances and those observed, suggest that the destruction of odd-oxygen by odd-hydrogen is less active on Mars than in current GCM simulations, which do not incorporate heterogeneous chemistry. This may be possibly due to differences in odd-hydrogen production rates, or the reaction rates involving odd-hydrogen species. This will have important implications for the photochemical cycles of water vapour and CO, as well as trace gases, such as HCl and methane.

Acknowledgments

The authors declare no conflicts of interest. The ACS investigation was developed by the Space Research Institute (IKI) in Moscow, and the Laboratoire Atmosphères, Milieux, Observations Spatiales (LATMOS/CNRS) in Paris. The investigation was funded by Roscosmos, the National Centre for Space Studies of France (CNES) and the Ministry of Science and Education of Russia. The GGG software suite is maintained at JPL (tccon-wiki.caltech.edu). This work was funded by the UK Space Agency (ST/T002069/1), the Natural Sciences and Engineering Research Council of Canada (NSERC) (PDF–516895–2018), and the National Centre for Space Studies of France (CNES). IKI affiliates acknowledge funding from the Russian Science Foundation (RSF-ANR 20-42-09035) (data analysis and interpretation). University of Oxford affiliates acknowledge funding from the UK Space Agency (ST/T002069/1, ST/R001502/1, and ST/P001572/1). LATMOS affiliates acknowledge funding from CNES and ANR (PRCI, CE31 AAPG2019-MCUBE project). All spectral fitting of ACS MIR data was performed by K.S.O. using the GGG software suite. Temperature and pressure data were provided by A.A.F. Processing of ACS spectra is done by A.T. at IKI and by L.B. at LATMOS by L.B. The LMD GCM data was generated by, and provided by, F.F., E.M., F.L., and A.B. Input and aid on spectral fitting, and on interpretation of data, were given by J.A., D.A.B., C.F.W., P.G.J.I., A.F., F.M., and F.L. The ACS instrument was designed, developed, and operated by A.P., A.S., A.T., F.M., and O.K.

Open Data

The VMR vertical profiles generated in this study are available on the Oxford Research Archive at dx.doi.org/10.5287/bodleian:2adPoRMdz. The data sets generated by the ExoMars Trace Gas Orbiter instruments analyzed in this study are made available in the ESA Planetary Science Archive (PSA) repository, https://archives.esac.esa.int/psa/#!Table%20View/ACS=instrument, following a six months prior access period, and the ESA Rules on Information, Data and Intellectual Property. Temperature and pressure data used here are from ACS NIR and were generated in other studies. Data from MY 34 are made available in Fedorova et al. (2020) and an updated data version containing MYs 34-36 are published in Fedorova et al. (2022). Data generated with the LMD GCM for TGO solar occultations, along with its user guide, are hosted

by LMD and can be found at: ftp://ftp.lmd.jussieu.fr/pub/forget/TGO_SO/. The subsets of both of these data sources used here are hosted on the Oxford Research Archive at dx.doi.org/10.5287/bodleian:b7xR5DPpJ.

References

Alday, J., Wilson, C. F., Irwin, P. G. J., Olsen, K. S., Baggio, L., Montmessin, F., et al. (2019). Oxygen isotopic ratios in Martian water vapour observed by ACS MIR on board the ExoMars Trace Gas Orbiter. *Astronomy & Astrophysics*, *630*, A91. https://doi.org/10.1051/0004-6361/201936234

Alday, J., Trokhimovskiy, A., Irwin, P. G. J., Wilson, C. F., Montmessin, F., Lefévre, F., et al. (2021). Isotopic fractionation of water and its photolytic products in the atmosphere of Mars. *Nature Astronomy*, *5*(9), 943–950. https://doi.org/10.1038/s41550-021-01389-x

Aoki, S., Vandaele, A. C., Daerden, F., Villanueva, G. L., Liuzzi, G., Thomas, I. R., et al. (2019). Water Vapor Vertical Profiles on Mars in Dust Storms Observed by TGO/NOMAD. *Journal of Geophysical Research: Planets*, *124*(12), 3482–3497. https://doi.org/10.1029/2019JE006109

Barth, C. A., & Hord, C. W. (1971). Mariner Ultraviolet Spectrometer: Topography and Polar Cap. *Science*, *173*(3993), 197–201. https://doi.org/10.1126/science.173.3993.197

Barth, C. A., Hord, C. W., Stewart, A. I., Lane, A. L., Dick, M. L., & Anderson, G. P. (1973). Mariner 9 Ultraviolet Spectrometer Experiment: Seasonal Variation of Ozone on Mars. *Science*, *179*(4075), 795–796. https://doi.org/10.1126/science.179.4075.795

Belyaev, D. A., Fedorova, A. A., Trokhimovskiy, A., Alday, J., Montmessin, F., Korablev, O. I., et al. (2021). Revealing a High Water Abundance in the Upper Mesosphere of Mars With ACS Onboard TGO. *Geophysical Research Letters*, *48*(10), e2021GL093411. https://doi.org/10.1029/2021GL093411

Clancy, R. T., & Nair, H. (1996). Annual (perihelion-aphelion) cycles in the photochemical behavior of the global Mars atmosphere. *Journal of Geophysical Research: Planets*, *101*(E5), 12785–12790. https://doi.org/10.1029/96JE00836

Clancy, R. T., Wolff, M. J., James, P. B., Smith, E., Billawala, Y. N., Lee, S. W., & Callan, M. (1996). Mars ozone measurements near the 1995 aphelion: Hubble space telescope ultraviolet spectroscopy with the faint object spectrograph. *Journal of Geophysical Research: Planets*, *101*(E5), 12777–12783. https://doi.org/10.1029/96JE00835

Clancy, R. T., Grossman, A. W., Wolff, M. J., James, P. B., Rudy, D. J., Billawala, Y. N., et al. (1996). Water Vapor Saturation at Low Altitudes around Mars Aphelion: A Key to Mars Climate? *Icarus*, *122*(1), 36–62. https://doi.org/10.1006/icar.1996.0108

Clancy, R. T., Wolff, M. J., Lefèvre, F., Cantor, B. A., Malin, M. C., & Smith, M. D. (2016). Daily global mapping of Mars ozone column abundances with MARCI UV band imaging. *Icarus*, *266*, 112–133. https://doi.org/10.1016/j.icarus.2015.11.016

Daerden, F., Neary, L., Viscardy, S., García Muñoz, A., Clancy, R. T., Smith, M. D., et al. (2019). Mars atmospheric chemistry simulations with the GEM-Mars general circulation model. *Icarus*, *326*, 197–224. https://doi.org/10.1016/j.icarus.2019.02.030

Devi, V. M., Benner, D. C., Sung, K., Crawford, T. J., Gamache, R. R., Renaud, C. L., et al. (2017). Line parameters for CO_2- and self-broadening in the $^{16\$}$O. *J. Quant. Spectrosc. Radiat. Transfer*, *203*, 158–174. https://doi.org/10.1016/j.jqsrt.2017.02.020

Espenak, F., Mumma, M. J., Kostiuk, T., & Zipoy, D. (1991). Ground-based infrared measurements of the global distribution of ozone in the atmosphere of Mars. *Icarus*, *92*(2), 252–262. https://doi.org/10.1016/0019-1035(91)90049-Y

Fast, K., Kostiuk, T., Espenak, F., Annen, J., Buhl, D., Hewagama, T., et al. (2006). Ozone abundance on Mars from infrared heterodyne spectra. I. Acquisition, retrieval, and anticorrelation with water vapor. *Icarus*, *181*(2), 419–431. https://doi.org/10.1016/j.icarus.2005.12.001

Fedorova, A. A., Montmessin, F., Korablev, O., Luginin, M., Trokhimovskiy, A., Belyaev, D. A., et al. (2020). Stormy water on Mars: The distribution and saturation of atmospheric water during the dusty season. *Science*, *367*(6475), 297–300. https://doi.org/10.1126/science.aay9522

Fedorova, A. A., Montmessin, F., Korablev, O., Lefèvre, F., Trokhimovskiy, A., & Bertaux, J.-L. (2021). Multi-Annual Monitoring of the Water Vapor Vertical Distribution on Mars by SPICAM on Mars Express. *Journal of Geophysical Research: Planets*, *126*(1), e2020JE006616. https://doi.org/10.1029/2020JE006616

Fedorova, A. A., Montmessin, F., Trokhimovskiy, A., Luginin, M., Korablev, O., Alday, J., et al. (2022). A two-Martian year survey of the water vapor saturation state on Mars based on ACS NIR/TGO occultations. *J. Geophys. Res.*

Forget, F., Hourdin, F., Fournier, R., Hourdin, C., Talagrand, O., Collins, M., et al. (1999). Improved general circulation models of the Martian atmosphere from the surface to above 80 km. *J. Geophys. Res.*, *104*, 24155–24176. https://doi.org/10.1029/1999JE001025

Gamache, R. R., Farese, M., & Renaud, C. L. (2016). A spectral line list for water isotopologues in the 1100-4100 $cm^{-1\$}$ region for application to CO_2-rich planetary atmospheres. *J. Mol. Spectrosc.*, *326*, 144–150. https://doi.org/10.1016/j.jms.2015.09.001

Gordon, I. E., Rothman, L. S., Hargreaves, R. J., Hashemi, R., Karlovets, E. V., Skinner, F. M., et al. (2021). The HITRAN2020 molecular spectroscopic database. *Journal of Quantitative Spectroscopy and Radiative Transfer*, 107949. https://doi.org/10.1016/j.jqsrt.2021.107949

Irion, F. W., Gunson, M. R., Toon, G. C., Chang, A. Y., Eldering, A., Mahieu, E., et al. (2002). Atmospheric Trace Molecule Spectroscopy (ATMOS) Experiment Version 3 data retrievals. *Appl. Opt.*, *41*, 6968–6979. https://doi.org/10.1364/AO.41.006968

Khayat, A. S. J., Smith, M. D., Wolff, M., Daerden, F., Neary, L., Patel, M. R., et al. (2021). ExoMars TGO/NOMAD-UVIS vertical profiles of ozone: Part 2: The high-altitude layers of atmospheric ozone. *Journal of Geophysical Research: Planets*, e2021JE006834. https://doi.org/10.1029/2021JE006834

Korablev, O., Montmessin, F., Trokhimovskiy, A., Fedorova, A. A., Shakun, A. V., Grigoriev, A. V., et al. (2018). The Atmospheric Chemistry Suite (ACS) of Three Spectrometers for the ExoMars 2016 Trace Gas Orbiter. *Space Science Reviews*, *214*(1), 7. https://doi.org/10.1007/s11214-017-0437-6

Korablev, O., Vandaele, A. C., Montmessin, F., Fedorova, A. A., Trokhimovskiy, A., Forget, F., et al. (2019). No detection of methane on Mars from early ExoMars Trace Gas Orbiter observations. *Nature*, *568*, 517–520. https://doi.org/10.1038/s41586-019-1096-4

Korablev, O., Olsen, K. S., Trokhimovskiy, A., Lefèvre, F., Montmessin, F., Fedorova, A. A., et al. (2021). Transient HCl in the atmosphere of Mars. *Science Advances*, *7*(7), eabe4386. https://doi.org/10.1126/sciadv.abe4386

Lebonnois, S., Quémerais, E., Montmessin, F., Lefèvre, F., Perrier, S., Bertaux, J.-L., & Forget, F. (2006). Vertical distribution of ozone on Mars as measured by SPICAM/Mars Express using stellar occultations. *J. Geophys. Res.*, *111*(E9), E09S05. https://doi.org/10.1029/2005JE002643

Lefèvre, F., & Krasnopolsky, V. (2017). Atmospheric Photochemistry. In R. M. Haberle, R. T. Clancy, F. Forget, M. D. Smith, & R. W. Zurek (Eds.), *The Atmosphere and Climate of Mars* (pp. 405–432). Cambridge University Press.

Lefèvre, F., Lebonnois, S., Montmessin, F., & Forget, F. (2004). Three-dimensional modeling of ozone on Mars. *J. Geophys. Res.*, *109*(E7), E07004. https://doi.org/10.1029/2004JE002268

Lefèvre, F., Trokhimovskiy, A., Fedorova, A., Baggio, L., Lacombe, G., Määttänen, A., et al. (2021). Relationship Between the Ozone and Water Vapor Columns on Mars as Observed by SPICAM and Calculated by a Global Climate Model. *Journal of Geophysical Research: Planets*, *126*(4), e2021JE006838. https://doi.org/10.1029/2021JE006838

Luginin, M., Fedorova, A., Ignatiev, N., Trokhimovskiy, A., Shakun, A., Grigoriev, A., et al. (2020). Properties of Water Ice and Dust Particles in the Atmosphere of Mars During the 2018 Global Dust Storm as Inferred From the Atmospheric Chemistry Suite. *Journal of Geophysical Research: Planets*, *125*(11), e2020JE006419. https://doi.org/10.1029/2020JE006419

Madeleine, J.-B., Forget, F., Spiga, A., Wolff, M. J., Montmessin, F., Vincendon, M., et al. (2012). Aphelion water-ice cloud mapping and property retrieval using the OMEGA imaging spectrometer onboard Mars Express. *J. Geophys. Res.*, *117*, E00J07. https://doi.org/10.1029/2011JE003940

Mitchell, D. M., Montabone, L., Thomson, S., & Read, P. L. (2015). Polar vortices on Earth and Mars: A comparative study of the climatology and variability from reanalyses. *Quarterly Journal of the Royal Meteorological Society*, *141*(687), 550–562. https://doi.org/10.1002/qj.2376

Montabone, L., Forget, F., Millour, E., Wilson, R. J., Lewis, S. R., Cantor, B., et al. (2015). Eight-year climatology of dust optical depth on Mars. *Icarus*, *251*, 65–95. https://doi.org/10.1016/j.icarus.2014.12.034

Montabone, L., Spiga, A., Kass, D. M., Kleinböhl, A., Forget, F., & Millour, E. (2020). Martian Year 34 Column Dust Climatology from Mars Climate Sounder Observations: Reconstructed Maps and Model Simulations. *J. Geophys. Res.*

Montmessin, F., & Lefèvre, F. (2013). Transport-driven formation of a polar ozone layer on Mars. *Nature Geoscience*, *6*(11), 930–933. https://doi.org/10.1038/ngeo1957

Navarro, T., Madeleine, J.-B., Forget, F., Spiga, A., Millour, E., Montmessin, F., & Määttänen, A. (2014). Global

climate modeling of the Martian water cycle with improved microphysics and radiatively active water ice clouds. *J. Geophys. Res.*, *119*, 1479–1495. https://doi.org/10.1002/2013JE004550

Olsen, K. S., Lefèvre, F., Montmessin, F., Trokhimovskiy, A., Baggio, L., Fedorova, A., et al. (2020). First detection of ozone in the mid-infrared at Mars: implications for methane detection. *Astron. Astrophys. in Press*. https://doi.org/10.1051/0004-6361/202038125

Olsen, K. S., Trokhimovskiy, A., Montabone, L., Fedorova, A. A., Luginin, M., Lefèvre, F., et al. (2021). Seasonal reappearance of HCl in the atmosphere of Mars during the Mars year 35 dusty season. *Astronomy & Astrophysics*, *647*, A161. https://doi.org/10.1051/0004-6361/202140329

Olsen, K. S., Lefèvre, F., Montmessin, F., Fedorova, A. A., Trokhimovskiy, A., Baggio, L., et al. (2021). The vertical structure of CO in the Martian atmosphere from the ExoMars Trace Gas Orbiter. *Nature Geoscience*, *14*(2), 67–71. https://doi.org/10.1038/s41561-020-00678-w

Olsen, K. S., Trokhimovskiy, A., Braude, A. S., Korablev, O., Fedorova, A. A., Wilson, C. F., et al. (2021). Upper limits for phosphine (PH3) in the atmosphere of Mars. *Astronomy & Astrophysics*, *649*, L1. https://doi.org/10.1051/0004-6361/202140868

Patel, M. R., Sellers, G., Mason, J. p., Holmes, J. A., Brown, M. A. J., Lewis, S. R., et al. (2021). ExoMars TGO/NOMAD-UVIS vertical profiles of ozone: Part 1 – Seasonal variation and comparison to water. *Journal of Geophysical Research: Planets*, e2021JE006837. https://doi.org/10.1029/2021JE006837

Pearl, J. C., Smith, M. D., Conrath, B. J., Bandfield, J. L., & Christensen, P. R. (2001). Observations of Martian ice clouds by the Mars Global Surveyor Thermal Emission Spectrometer: The first Martian year. *J. Geophys. Res.*, *106*, 12325–12338. https://doi.org/10.1029/1999JE001233

Perrier, S., Bertaux, J. L., Lefèvre, F., Lebonnois, S., Korablev, O., Fedorova, A., & Montmessin, F. (2006). Global distribution of total ozone on Mars from SPICAM/MEX UV measurements. *J. Geophys. Res.*, *111*(E9). https://doi.org/10.1029/2006JE002681

Smith, M. D. (2004). Interannual variability in TES atmospheric observations of Mars during 1999-2003. *Icarus*, *167*, 148–165. https://doi.org/10.1016/j.icarus.2003.09.010

Stcherbinine, A., Vincendon, M., Montmessin, F., Wolff, M. J., Korablev, O., Fedorova, A., et al. (2020). Martian Water Ice Clouds During the 2018 Global Dust Storm as Observed by the ACS-MIR Channel Onboard the

Trace Gas Orbiter. *Journal of Geophysical Research: Planets*, *125*(3), e2019JE006300. https://doi.org/10.1029/2019JE006300

Trokhimovskiy, A., Perevalov, V., Korablev, O., Fedorova, A. F., Olsen, K. . S., Bertaux, J.-L., et al. (2020). First observation of the magnetic dipole CO_2 main isotopologue absorption band at 3.3 μm in the atmosphere of Mars by ACS. *Astron. Astrophys. in Press*. https://doi.org/10.1051/0004-6361/202038134

Tudorie, M., Földes, T., Vandaele, A. C., & Vander Auwera, J. (2012). CO2 pressure broadening and shift coefficients for the 1–0 band of HCl and DCl. *Journal of Quantitative Spectroscopy and Radiative Transfer*, *113*(11), 1092–1101. https://doi.org/10.1016/j.jqsrt.2012.01.025

Waugh, D. W., Toigo, A. D., Guzewich, S. D., Greybush, S. J., Wilson, R. J., & Montabone, L. (2016). Martian polar vortices: Comparison of reanalyses. *Journal of Geophysical Research: Planets*, *121*(9), 1770–1785. https://doi.org/10.1002/2016JE005093

Wilzewski, J. S., Gordon, I. E., Kochanov, R. V., Hill, C., & Rothman, L. S. (2016). H_2, He, and CO_2 line-broadening coefficients, pressure shifts and temperature-dependence exponents for the HITRAN database. Part 1: SO_2, NH_3, HF, HCl, OCS and C_2H_2. *J. Quant. Spectrosc. Radiat. Transfer*, *168*, 193–206. https://doi.org/10.1016/j.jqsrt.2015.09.003

Wunch, D., Toon, G. C., Blavier, J. L., Washenfelder, R. A., Notholt, J., Connor, B. J., et al. (2011). The Total Carbon Column Observing Network. *Phil. Trans. R. Soc. A*, *369*, 2087–2112. https://doi.org/10.1098/rsta.2010.0240